

Binary black hole mergers from young massive clusters in the pair-instability supernova mass gap

Sambaran Banerjee ^{*1,2}

¹ Helmholtz-Instituts für Strahlen- und Kernphysik, Nussallee 14-16, D-53115 Bonn, Germany

² Argelander-Institut für Astronomie, Auf dem Hügel 71, D-53121, Bonn, Germany

June 15, 2022

ABSTRACT

Context. The recent discovery of the binary black hole (BBH) merger event GW190521, between two black holes (BHs) of $\approx 100M_{\odot}$, and as well as other massive BBH merger events involving BHs within the pair-instability supernova (PSN) mass gap have sparked widespread debate on the origin of such extreme gravitational-wave (GW) events. GW190521 simultaneously triggers two critical questions: how BHs can appear within the ‘forbidden’ PSN gap and, if so, how they get to participate in general-relativistic (GR) mergers?

Aims. In this study, I investigate whether dynamical interactions in young massive clusters (YMCs) serve as a viable scenario for assembling PSN-gap BBH mergers.

Methods. To that end, I explore a grid of 40 new evolutionary models of a representative YMC of initial mass and size $M_{cl} = 7.5 \times 10^4 M_{\odot}$ ($N \approx 1.28 \times 10^5$) and $r_h = 2$ pc, respectively. The model grid ranges over metallicity $0.0002 \leq Z \leq 0.02$ and comprises initial cluster configurations of King central concentration parameters $W_0 = 7$ and 9. In each model, all BH progenitor stars are initially in primordial binaries following observationally-motivated distributions. All cluster models are evolved with the direct, relativistic N-body code NBODY7 incorporating up to date remnant formation, BH natal spin, and GR merger recoil schemes.

Results. BBH mergers from these model cluster computations agree well with the masses and effective spin parameters, χ_{eff} , of the events from the latest gravitational-wave transient catalogue (GWTC). In particular, GW190521-like, *i.e.*, $\approx 200M_{\odot}$, low χ_{eff} events are produced via dynamical merger among BHs derived from star-star merger products. GW190403_051519-like, *i.e.*, PSN-gap, highly asymmetric, high χ_{eff} events result from mergers involving BHs that are spun up via matter accretion or binary interaction. The resulting present-day, differential intrinsic merger rate density, within the PSN gap, well accommodates that from GWTC.

Conclusions. This study demonstrates that, subject to model uncertainties, the tandem of massive binary evolution and dynamical interactions in $\lesssim 100$ Myr-old, low metallicity YMCs in the Universe can plausibly produce GR mergers involving PSN-gap BHs and in rates consistent with that from to-date GW observations. Such clusters can produce extreme events alike GW190521 and GW190403_051519. The upper limit of the models’ GW190521-type event rate is within the corresponding LIGO-Virgo-KAGRA (LVK)-estimated rate limits, although the typical model rate lies below the LVK’s lower limit. The present YMC models yield a merger rate density of $0 - 3.8 \times 10^{-2} \text{ yr}^{-1} \text{ Gpc}^{-3}$ for GW190521-type events. They produce GW190403_051519-like events at a rate within $0 - 1.6 \times 10^{-1} \text{ yr}^{-1} \text{ Gpc}^{-3}$ and their total BBH-merger yield within the PSN gap is $0 - 8.4 \times 10^{-1} \text{ yr}^{-1} \text{ Gpc}^{-3}$.

Key words. Stars: black holes — Stars: massive — Stars: kinematics and dynamics — supernovae: general — Methods: numerical — Gravitational waves

1. Introduction

Within just a few years after the first detection (Abbott et al. 2016) of gravitational wave (hereafter GW) from a merging binary black hole (hereafter BBH), we are already approaching a ‘golden era’ of GW and multi-messenger astronomy (Branchesi 2016; Mapelli 2018; Mészáros et al. 2019; Mandel & Broekgaarden 2022). Recently, the LIGO-Virgo-KAGRA collaboration (hereafter LVK; Aasi et al. 2015; Acernese et al. 2015; KAGRA Collaboration et al. 2020) has published, in their GW transient catalogue (hereafter GWTC) ¹, about 90 candidates of general relativistic (hereafter GR) compact binary merger events from until the end of their third observing run, ‘O3’. The up to date GWTC includes all event candidates from the LVK’s first, second (‘O1’, ‘O2’; Abbott et al. 2019), and third (‘O3’; Abbott et al. 2021a; The LIGO Scientific Collaboration et al. 2021b) ob-

serving runs including those in their ‘Deep Extended Catalogue’ (The LIGO Scientific Collaboration et al. 2021a).

GWTC contains several events that have triggered widespread debate regarding the events’ origin or formation channel. Perhaps the most explored event, since its announcement, is GW190521 (Abbott et al. 2020): a merger of two black holes (hereafter BHs) of estimated masses $M_1 = 95.3^{+28.7}_{-18.9} M_{\odot}$ and $M_2 = 69.0^{+22.7}_{-23.1} M_{\odot}$ and effective aligned spin parameter $\chi_{\text{eff}} = 0.03^{+0.32}_{-0.39}$ (Abbott et al. 2021a; the limits correspond to 90% credibility). χ_{eff} (Ajith et al. 2011) is a measure of the spin-orbit alignment of a merging binary and is defined as

$$\chi_{\text{eff}} \equiv \frac{M_1 a_1 \cos \theta_1 + M_2 a_2 \cos \theta_2}{M_1 + M_2} = \frac{a_1 \cos \theta_1 + q a_2 \cos \theta_2}{1 + q}. \quad (1)$$

Here, the GR-inspiralling masses M_1 , M_2 , with mass ratio $q \equiv M_2/M_1$, have, respectively, Kerr vectors \mathbf{a}_1 , \mathbf{a}_2 that project with angles θ_1 , θ_2 on the orbital angular momentum vector just before the merger. The Kerr vector or Kerr parameter (also addressed

* Corresponding author. E-mail: sambaran@astro.uni-bonn.de (he/him/his)

¹ <https://www.gw-openscience.org/eventapi/html/GWTC/>

as dimensionless spin vector or dimensionless spin parameter), \mathbf{a} , is defined as (Kerr 1963)

$$\mathbf{a} = \frac{c\mathbf{S}_{\text{BH}}}{GM_{\text{BH}}^2} \quad (2)$$

where \mathbf{S}_{BH} is the total angular momentum vector of a Kerr BH of (non-spinning) mass M_{BH} .

Another notable PSN-gap event is GW190403_051519 (hereafter GW190403) which is lighter than GW190521 but, in contrast, is highly mass-asymmetric ($M_1 = 88.0^{+28.2}_{-32.9}M_{\odot}$, $M_2 = 22.1^{+23.8}_{-9.0}M_{\odot}$) and spin-orbit aligned ($\chi_{\text{eff}} = 0.70^{+0.15}_{-0.27}$). GW190426_190642 has masses and χ_{eff} similar to GW190521 although this event is of much higher false alarm rate (hereafter FAR), 4.1 yr^{-1} , as opposed to $\text{FAR} = 2 \times 10^{-4} \text{ yr}^{-1}$ for GW190521. The current GWTC includes several additional candidates of BBH mergers with the primary being within the PSN gap.

The excitement is natural since both components of this BBH merger lie well within the ‘forbidden’ pair-instability supernova (hereafter PSN) mass gap between $45M_{\odot} \lesssim M_{\text{rem}} \lesssim 120M_{\odot}$ (Belczynski et al. 2016; Woosley 2017). Starting to evolve from their zero age main sequence (hereafter ZAMS), massive single stars are not expected to produce any compact remnant over this remnant-mass range and, instead, explode completely due to PSN occurring in their late evolutionary stages (Langer et al. 2007; Woosley 2017; Mapelli et al. 2020). The lower limit of the PSN gap occurs due pulsation pair-instability supernova (hereafter PPSN) that episodically sheds the hydrogen envelope of the parent star until a helium core of $\approx 45M_{\odot}$ is retained (Woosley 2017; Woosley et al. 2020) which then directly collapses into a BH. The upper limit of the gap results when the progenitor star becomes massive enough that PPSN and PSN quenches (see, e.g., Ziegler & Freese 2021) and the evolved star can directly collapse into an intermediate mass BH (hereafter IMBH). See Fig. 2 of Banerjee et al. (2020) for the ‘standard’ ZAMS mass-final mass relation, exhibiting the PSN gap at different metallicities.

Therefore, the observation of BHs within the PSN gap, at least at a first glance, is a signature of an outlier BH population (Baibhav et al. 2021; O’Brien et al. 2021) and intrigues more exotic scenarios of BH formation and merger. Several scenarios have already been invoked to explain GW190521-type events: primordial BHs (e.g., Clesse & García-Bellido 2017; Carr & Silk 2018; De Luca et al. 2019), BHs derived from Population III stars (e.g., Tanikawa et al. 2021b,a; Ziegler & Freese 2021), gas accretion onto BHs in dense proto-clusters (e.g., Roupas & Kazanas 2019), GR coalescences in field hierarchical systems (e.g., Fragione et al. 2020; Vigna-Gómez et al. 2021; Hamers et al. 2021), and stellar collisions and dynamical interactions inside dense stellar clusters.

In this study, a young massive cluster (hereafter YMC) origin of PSN-gap BBH mergers is investigated. Dynamical interactions among stellar-remnant BHs inside dense star clusters is an intriguing scenario for generating PSN-gap and other types of massive BBH mergers (Perna et al. 2019; Arca Sedda et al. 2020; Baibhav et al. 2020; Banerjee 2021a; Rizzuto et al. 2021, 2022; Gerosa & Fishbach 2021; Mapelli et al. 2021) since the scenario naturally allows for prolonged post-processing of BHs and BBHs formed as a result of massive binary evolution. Dynamical interactions also enable star-star and star-remnant mergers of kinds which would not be possible with the evolution of isolated massive binaries alone (Di Carlo et al. 2020b; González et al. 2021; Rastello et al. 2021). Such interactions would potentially

lead to ‘forbidden’ BHs and mergers involving them, depending on the cluster’s properties and its stellar and multiplicity content. Since the most massive members in a star cluster undergo dynamical processing the earliest, the most massive BBH mergers are expected to occur early in the cluster’s evolution (Banerjee 2017). As shown in earlier works (Banerjee et al. 2010; Banerjee 2017; Rodriguez et al. 2018), dynamical BBH mergers in a YMC can occur inside the cluster due to hierarchical-system interactions (e.g., Kozai–Lidov oscillation, chaotic triple-interaction; Kozai 1962; Katz et al. 2011; Lithwick & Naoz 2011) or close flyby interactions, within the centrally segregated BH subsystem (Banerjee et al. 2010; Morscher et al. 2015). A fraction of the BBHs (and other types of compact binaries) ejected from the cluster, either dynamically or due to natal kick, can also merge within the Hubble time (Sigurdsson & Hernquist 1993; Portegies Zwart & McMillan 2000).

It should, however, be borne in mind that it is possible that the ‘standard’ PSN mass gap (see above) is simply an artefact of the ‘standard’ theoretical stellar evolution models. The PPSN mass cap can potentially be much higher or the PSN mass gap can even be nonexistent. This is supported by both stellar evolutionary models (Belczynski et al. 2020a; Farmer et al. 2020; Woosley & Heger 2021; Vink et al. 2021; Costa et al. 2021) and the observed population of merging BHs (The LIGO Scientific Collaboration et al. 2021c; Edelman et al. 2021). In that case, GW190521-like events can simply be explained by the standard isolated binary evolution scenario (Belczynski 2020). The present study bases on the existence of the standard PSN gap and involves a stellar-remnant model that exhibits such a gap.

This paper is organized as follows. Sec. 2 describes a new set of direct N-body computations of model YMCs. Sec. 3 discusses the outcomes, focussing on PSN-gap mergers. Sec. 3.1 describes the inferred rate of GW190521-like events and Sec. 3.2 covers that of GW190403-like mergers. Sec. 4 summarizes the findings and discusses the implications of various model assumptions and the limitations.

2. Computations

Close dynamical interactions, star-star mergers, and star-remnant mergers are generally favoured in massive star clusters having profiles of high central concentration. This is due to the resulting high central stellar density and efficient mass segregation. Therefore, massive BH formation and their mergers can be expected to preferably occur in such systems. Since massive, PSN-gap BH formation and their involvement in GR mergers is the focus of this study, massive, concentrated model clusters are specifically considered. In this work, model star clusters with initial mass of $M_{\text{cl}} = 7.5 \times 10^4 M_{\odot}$ (initial number of stars $N \approx 1.28 \times 10^5$) are taken to be representatives of YMCs. Such a cluster mass is comparable to those of most massive Galactic and local-group YMCs. It is also representative of moderate mass ‘super star clusters’ (Portegies Zwart et al. 2010). The stellar content of these star cluster models is motivated by the cluster models described in Banerjee (2021a, hereafter Ba21). The initial density and kinematic profiles of the clusters follow the King (1966) model with half-mass radius $r_h = 2 \text{ pc}$ and King dimensionless potential of $W_0 = 7$ and 9. Such size is typical for YMCs (Portegies Zwart et al. 2010; Krumholz et al. 2019).

Previous results in Ba21 and Banerjee (2021b), where the models use the Plummer (1911) initial conditions, *i.e.*, with the central concentration comparable to $W_0 \approx 5 - 6$ (Heggie & Hut 2003), suggest that massive clusters ($M_{\text{cl}} \geq 5 \times 10^4 M_{\odot}$) are capable of producing and merging PSN-gap BHs. An objective of

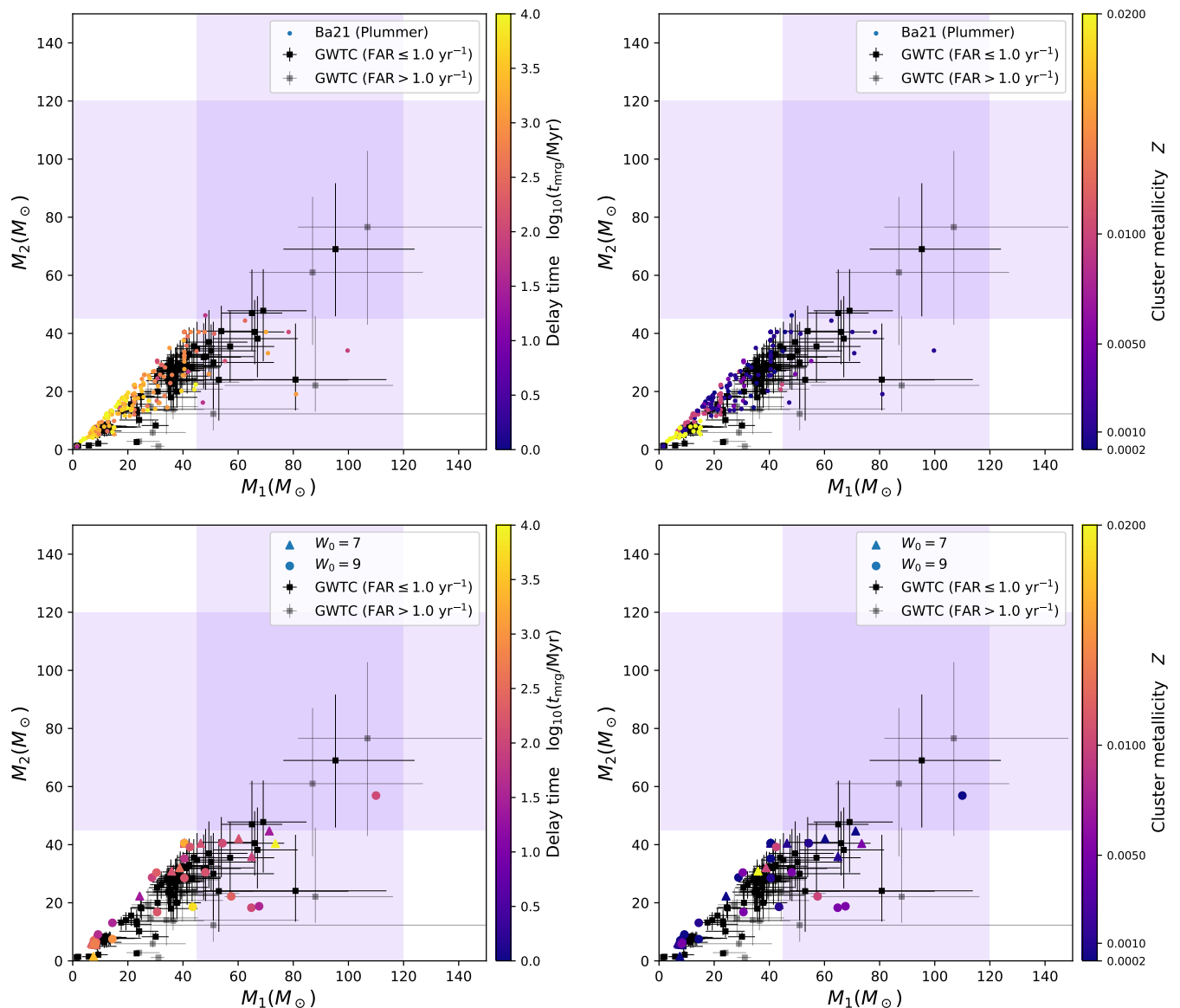


Fig. 1. Top panels: primary mass, M_1 , versus secondary mass, M_2 ($M_1 \geq M_2$), of all BBH mergers from the computed model star clusters of Ba21 (filled circles). These data points are colour-coded according to the merger delay time, t_{mrg} (left panel), and the parent model cluster’s metallicity, Z (right panel). The GWTC events’ data points (black, filled squares) and their corresponding 90% credible intervals (horizontal and vertical error bars) are indicated, where events with $\text{FAR} \leq 1.0 \text{ yr}^{-1}$ and $> 1.0 \text{ yr}^{-1}$ are distinguished by different shades. The blue-shaded regions over $45M_\odot - 120M_\odot$ on each panel represent the PSN mass gap. (The blue shadings are placed in the background so that they do not influence the colours of the data points.) **Bottom panels:** the same as the top panels except that the mergers from the present computed clusters (Table A.1) with King concentration parameters $W_0 = 7.0$ (filled triangles) and 9.0 (filled circles) are shown.

the present study is to see how somewhat more centrally peaked initial models fair in this which is why $W_0 = 7$ and 9 are chosen here (less concentrated model would be uninteresting in this regard due to the reasons given above). The King profile offers the freedom to alter the central concentration without altering the cluster’s overall length scale (as measured by r_h).

Another objective is to see how pc-scale clusters fair as opposed to highly concentrated, sub-pc-scale clusters of r_h comparable to widths of molecular-cloud filaments, the latter conditions having been recently studied by several authors (Di Carlo et al. 2020b; Rastello et al. 2021; Rizzuto et al. 2022). (Near) monolithic, (near) gas-free, pc-scale YMCs are something that we do observe and can measure with relative unambiguity in various surveys (Mathieu 2000; Portegies Zwart et al. 2010; Kuhn et al. 2013; Krumholz et al. 2019). The gas-free nature of such

clusters implies that any potential violent-relaxation phase and its impact on the cluster (Banerjee & Kroupa 2018) can be ignored and the cluster can be assumed to evolve solely via secular dynamical evolution, as is the case with the present model clusters.

As in Ba21, the initial models are composed of ZAMS stars of masses $0.08M_\odot \leq m_* \leq 150.0M_\odot$ that are distributed according to the canonical initial mass function (hereafter IMF; Kroupa 2001) and have an overall (see below) primordial-binary fraction of $f_{\text{bin}} = 5\%$. However, as in Ba21, the initial binary fraction of the O-type stars ($m_* \geq 16.0M_\odot$), which are initially paired only among themselves, is taken to be $f_{\text{Obin}}(0) = 100\%$, to be consistent with the observed high binary fraction among O-stars in young clusters and associations (e.g., Sana & Evans 2011; Sana et al. 2013; Moe & Di Stefano 2017). The O-star binaries are

taken to initially follow the observed orbital-period distribution of Sana & Evans (2011) and a uniform mass-ratio distribution. The initial orbital periods of the non-O-star primordial binaries follow the period distribution of Duquennoy & Mayor (1991) and their mass-ratio distribution is also uniform. The initial eccentricity of the O-star binaries follows the Sana & Evans (2011) eccentricity distribution and that for the rest of the binaries obeys the thermal eccentricity distribution (Spitzer 1987). As explained in Banerjee (2018b), such a scheme for including primordial binaries provides a reasonable compromise between the economy of computing and consistencies with observations.

The model clusters are evolved with the star-by-star, direct N-body evolution code NBODY7 (Aarseth 2012), which is updated in several aspects as detailed in Banerjee et al. (2020, hereafter Ba20) and Ba21. These updates mainly enable up-to-date stellar wind mass loss and remnant formation in the code and as well implement numerical relativity (hereafter NR)-based GR merger recoil and spin recycling of merged BHs. The latter allows for on-the-fly and consistent treatment of BBH merger products. The primary ‘engine’ for stellar and binary evolution in NBODY7 is BSE (Hurley et al. 2000, 2002) and that for post-Newtonian (hereafter PN) evolution of compact binaries and higher order systems is ARCHAIN (Mikkola & Tanikawa 1999; Mikkola & Merritt 2008). In the present computed models, the ‘F12-rapid+B16-PPSN/PSN’ (see Ba20) remnant-mass prescription is applied. For single star evolution, this remnant prescription allows for the formation of stellar remnants, of mass M_{rem} , maintaining a neutron star (NS)-BH mass gap between $2M_{\odot} \lesssim M_{\text{rem}} \lesssim 5M_{\odot}$ (Fryer et al. 2012) and a PSN mass gap between $45M_{\odot} \lesssim M_{\text{rem}} \lesssim 120M_{\odot}$ (Belczynski et al. 2016; Woosley 2017; see also Fig. 2 of Ba20).

In the present computations, zero Kerr parameter is assigned to all BHs derived from single stars or from members of non-mass-transferring or non-interacting binaries, as per the BH-formation models of Fuller & Ma (2019) - the FM19 BH natal spin model. If, after formation, a BH undergoes matter accretion due to a BH-star merger or mass transfer in a binary or if a BH is born in a tidally-interacting (or symbiotic) binary, its Kerr parameter is set to the maximally spinning value of $a = 1$. In the event of a BH-star merger (the formation of a BH Thorne–Zytkow object, Thorne & Zytkow 1975 or BH-TZO), $f_{\text{TZ}} = 0.95$ fraction of the merging star’s mass is assumed to be accreted onto the BH. Also, in star-star mergers, $f_{\text{mrg}} = 0.2$ fraction of the secondary’s mass ($\leq 10\%$ of the total merging stellar mass) is assumed to be lost in the merger process (Gaburov et al. 2008; Glebbeek et al. 2009). In the present runs, the NR treatment is updated to the more recent GW-recoil formulae of Lousto et al. (2012) and final-spin formulae of Hofmann et al. (2016).

For each W_0 of the initial King profile, five metallicities are taken, namely, $Z = 0.0002, 0.001, 0.005, 0.01, \text{ and } 0.02$. Four random model realizations of each (W_0, Z) pair, which are subjected to a solar-neighborhood-like external field², are evolved for 300 Myr. These 40 newly computed models are listed in Table A.1.

3. Results

Fig. 1 (bottom panels) show the primary mass, M_1 , versus secondary mass, M_2 ($M_1 \geq M_2$), of the compact-binary mergers from the computed models. All these events are in-cluster or

² As seen in recent studies such as Webb & Sills (2021), the dynamical evolution of YMCs similar to the present models remains practically unaffected by large alterations to the galactocentric distance.

ejected BBH mergers, except for one that is an NS-BH merger. The BBH-merger masses are, overall, well consistent with those from GWTC (black, filled squares with error bars; events with $\text{FAR} \leq 1 \text{ yr}^{-1}$ and $> 1 \text{ yr}^{-1}$ are distinguished by different shades). The NS-BH merger is also consistent with the LVK-detected NS-BH merger events (Abbott et al. 2021b), as seen near the bottom left corners of Fig. 1 (bottom panels). For comparison, analogous plots are obtained from the computed models of Ba21 (Fig. 1; top panels) whose mergers show similarly good agreement with the LVK events.

The presently computed cluster models are more efficient in producing PSN-gap BBH mergers: the 40 models produce similar number of mergers with M_1 and/or M_2 within the gap as the 65 models of Ba21. This is due to the more centrally-peaked initial profiles of the present models (Sec. 2) than those of Ba21 (despite similar r_h for both model sets). However, in both sets, mergers involving a PSN-gap BH happen only in models with $Z \leq 0.005$ (Fig. 1). In the present models, BHs in the PSN gap appear due to (i) star-star mergers and (ii) BH-TZO accretion. Depending on the stellar-evolutionary age of the merging stars, a star-star merger can result in an over-massive H-envelope of the merged star while its He-core mass being below the PPSN/PSN threshold. With sufficient H-envelope mass, such a merged star would evolve into a direct-collapse BH within the PSN-gap (e.g., Spera et al. 2019; Banerjee et al. 2020; Di Carlo et al. 2020a). Such a remnant mass range is ‘forbidden’ for single stars evolving directly from ZAMS. The high, 95% BH-TZO accretion, as adopted here, would also push BHs into the PSN gap as a result of sufficiently massive BH-star mergers.

In the Ba21 models, a third channel has also produced PSN-gap BBH mergers in the model runs with FM19 (vanishing) BH natal spins, namely, second generation (hereafter 2G) mergers³. In those models, most 2G BBH mergers have happened with delay times $t_{\text{mrg}} > 300 \text{ Myr}$. In the present models, although a few 2G BHs remain in the clusters until the end of the runs at 300 Myr evolutionary time (the majority of the 2G BHs being ejected from their host clusters at their formation due to GW recoil kick; see Sec. 2), none of them could get involved in another merger by this time as can be expected based on the Ba21 models.

The most massive, GW190521-like merger obtained from the present model set (Fig. 1; bottom panels) is a 1G, in-cluster merger between two PSN-gap BHs, both of which are derived from star-star merger products. The merger happened in one of the $Z = 0.0002, W_0 = 9$ models. Fig. 2 plots the mass distributions of stellar remnants retained within the cluster at different evolutionary times, for all the 40 computed models. To improve counts over the mass bins and as well facilitate comprehension, distributions, at a given cluster age, from all the four models with a given W_0 and Z are combined in one histogram. The figure demonstrates the overall trend that the maximum mass of the BHs retained in a cluster at a given age increases with decreasing Z and increasing W_0 , as can be expected.

Fig. 3 plots the effective (aligned) spin parameter, χ_{eff} , of the GR mergers from the present models against their chirp mass, M_{chirp} (top panels), and primary mass (bottom panels). A merg-

³ In this work, BHs derived directly from the nuclear evolution of stellar progenitors will be called first generation or 1G BHs. If a 1G BH gains mass due to stellar matter accretion, it will still be 1G. A 1G+1G BBH merger will result in a 2G BH, a BBH merger involving at least one 2G BH will yield a 3G BH, and so on. This convention is often followed in the literature.

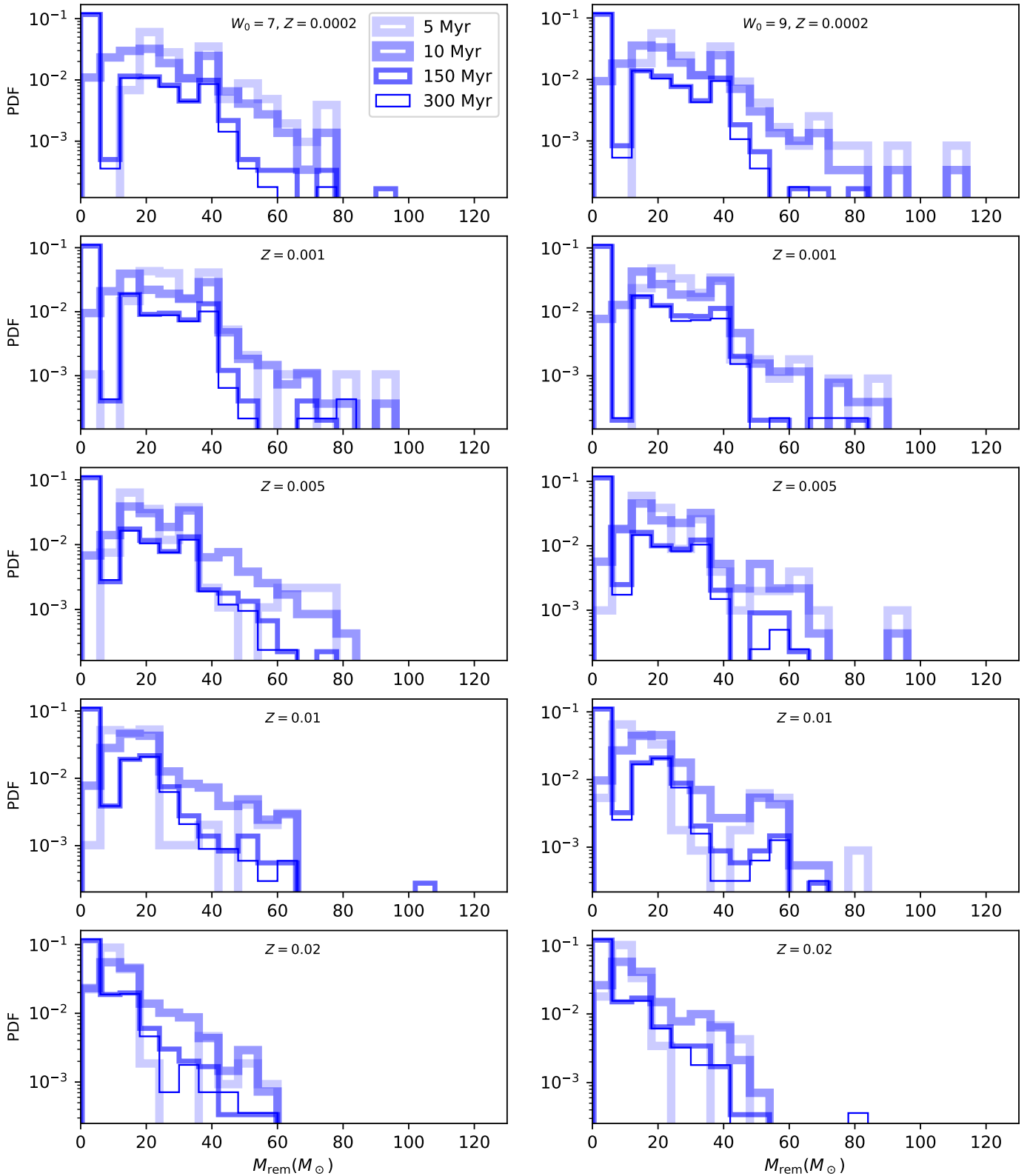


Fig. 2. The mass distributions of stellar remnants remaining in the computed model clusters (Table A.1) at 5 Myr, 10 Myr, 150 Myr, and 300 Myr cluster-evolutionary times (legend). The distributions, at a given time, from all (4) models for a particular W_0 and Z are combined in one histogram. The panels in the left (right) column correspond to the models with $W_0 = 7$ ($W_0 = 9$) with Z as indicated in each panel’s title.

ing system’s chirp mass is defined as

$$M_{\text{chirp}} \equiv \frac{(M_1 M_2)^{3/5}}{(M_1 + M_2)^{1/5}}. \quad (3)$$

For every GR merger from the computed models, a range of potential values of χ_{eff} is plotted in Fig. 3 by assigning independent, random values to θ_1 and θ_2 in Eqn. 1. If the components of the merging binary are derived from stellar progenitors that

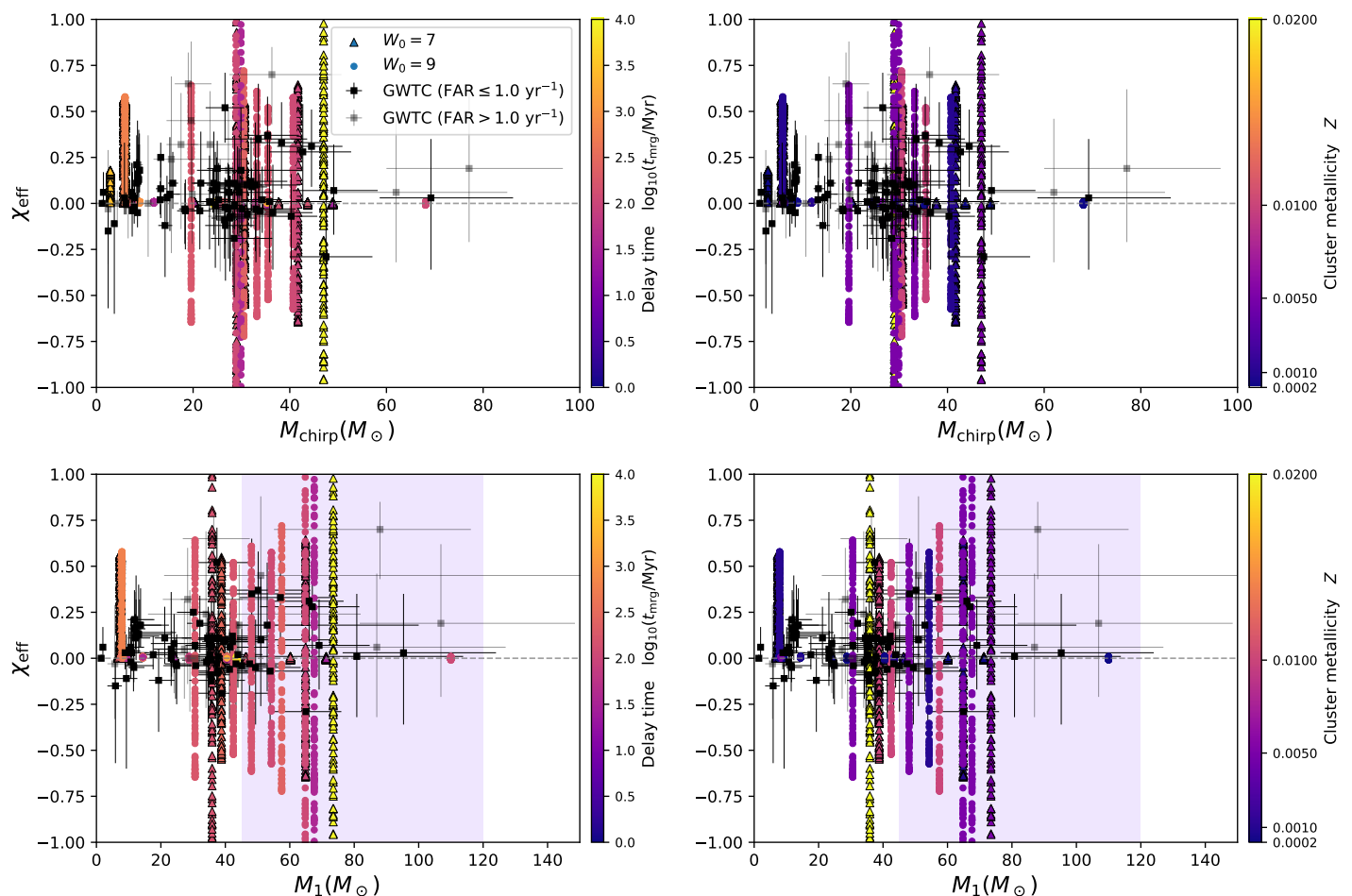


Fig. 3. Effective aligned spin parameter, χ_{eff} , versus chirp mass, M_{chirp} (top panels), and primary mass, M_1 (bottom panels), of all BBH mergers from the computed model clusters of Table A.1. For each merger, χ_{eff} values for a number of random orientations of the merging BHs’ spins are plotted (Sec. 3). The legends are the same as in Fig. 1 except that a black edge is applied to the filled triangle symbol for improved visibility.

were members of different primordial binaries or were initially single stars, *i.e.*, if the merging binary is dynamically assembled then the merging members are uncorrelated. Accordingly, (θ_1, θ_2) are taken to be isotropically oriented and values over the range $0 \leq (\theta_1, \theta_2) \leq 2\pi$ are assigned to them. On the other hand, if the merging components are derived from stellar progenitors that were members of the same primordial binary then they would, plausibly, be at least partially correlated. Therefore, in this case, values over the range $0 \leq (\theta_1, \theta_2) \leq \pi/2$ are assigned. For every merger from the models, the corresponding values of M_1, M_2, a_1, a_2 are taken directly from the model⁴.

For comparison, event data from GWTC are also plotted in Fig. 3. The LVK data points do exhibit an overall bias towards positive χ_{eff} , at least when the most probable values (squares) are considered. This is indicative of contribution from additional channels which tend to produce spin-aligned mergers, *e.g.*, isolated binary evolution. Mixing with additional channels will be addressed in a future work (see Banerjee 2022 in this context). Nevertheless, considering the 90% credible limits (error bars) the computed data points are consistent with the LVK data. In particular, the computed data well encompass the most massive

⁴ Special outputs are arranged in the updated NBODY7 for recording M_1, M_2, a_1, a_2 of the in-cluster and ejected mergers. In Fig. 3, each merger from the computed models is plotted with 100 random orientations of θ_1 and θ_2 . For the convenience of plotting, a small value of $a_i = 10^{-2}$ is assigned if $a_i = 0$.

observed PSN-gap mergers (of $M_1 \geq 55M_{\odot}$) with nearly vanishing, mildly aligned, and highly aligned χ_{eff} values.

Fig. 4 re-plots the model χ_{eff} as mean values with error bars, against M_1 (upper panels) and M_2 (lower panels), and highlights the events GW190521 and GW190403. Fig. 4 shows that the present model clusters produce only one GW190521-like and 5 GW190403-like events, in the sense that the model mergers’ $M_1, M_2,$ and χ_{eff} all lie within or enter the 90% credible intervals (the LVK-data error bars) of the respective parameters of these events of interest.

3.1. Rate of GW190521-like events

The present computed cluster models yield BBH mergers that well resemble notable PSN-gap events discovered by the LVK, in terms of, both, merging masses (M_1, M_2) and spin-orbit alignment (χ_{eff}). This is evident from Figs. 1, 3, and 4. The GW190521-like merger event is an outcome of an in-cluster, dynamically assembled and triggered merger between two BHs of $\approx 110M_{\odot}$ and $57M_{\odot}$, in one of the $Z = 0.0002, W_0 = 9$ models. Both of these BHs are formed due to evolution of star-star merger products with over-massive H-envelope (see above): both of these stellar mergers happened between components of massive primordial binaries. Since the BHs are derived directly from the (merged) stellar progenitors, they have zero natal spins as per the adopted BH natal spin model (Sec. 2). After form-

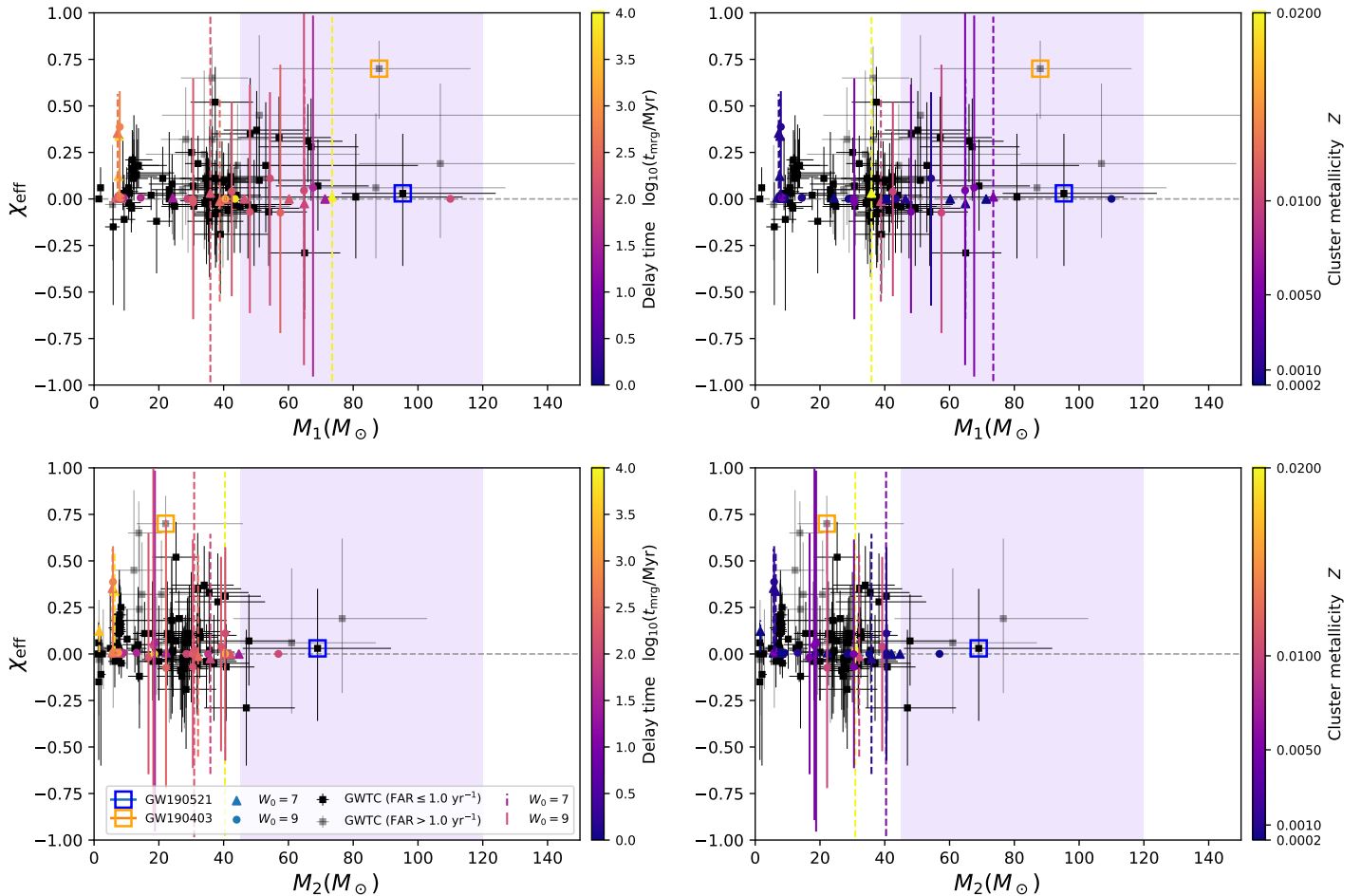


Fig. 4. Effective aligned spin parameter, χ_{eff} , versus primary mass, M_1 (top panels), and secondary mass, M_2 (bottom panels), of all BBH mergers from the computed model clusters of Table A.1. For each model merger, χ_{eff} values for a number of random orientations of the merging BHs’ spins are obtained (Sec. 3) which are shown as a data point (mean value) with a vertical error bar (range). The legends of the data points are the same as in Fig. 1. The error bars (in dashed line and solid line for mergers from the $W_0 = 7$ and $W_0 = 9$ models, respectively) share the same colour code as the corresponding data points. The LVK events GW190521 and GW190403 are highlighted with two empty squares (which are coloured differently for improved legibility and do not correspond to the color code).

ing as single BHs, they eventually get paired up via exchange interactions and merge due to a dynamical triple-interaction (Banerjee 2018a), resulting in an event with masses and χ_{eff} well within the 90%-credible limits of those of GW190521 and GW190426_190642. The detailed timeline of this event, from the formation of the merging BHs up to their merger, is depicted in Fig. 5 based on data directly from the N-body simulation and is described further in the figure’s caption.

The merger events from the present computed models are utilized to evaluate the differential merger rate density within the PSN gap. This is done by applying the same cluster population synthesis approach as described in Banerjee (2021b). The methodology is detailed in this reference which, therefore, is not repeated here. In the present application, a computed $M_{\text{cl}} = 7.5 \times 10^4 M_{\odot}$ cluster is taken as the representative YMC. Accordingly, when applying Eqn. 5 of Banerjee (2021b) the YMC birth mass range is taken to be $[M_{\text{cl,low}}, M_{\text{cl,high}}] = [5.7 \times 10^4 M_{\odot}, 10^5 M_{\odot}]$. This gives an average cluster mass of $\langle M_{\text{cl}} \rangle = 7.5 \times 10^4 M_{\odot}$ for a power-law cluster mass function of index $\alpha = -2$.

Population syntheses are performed with the merger outcomes from 4 different model sets having $[W_0 = 7 : Z = 0.0002, 0.001, 0.005, 0.01, 0.02]$ and 4 different model sets having $[W_0 = 9 : Z = 0.0002, 0.001, 0.005, 0.01, 0.02]$ (Table A.1).

With each cluster model set, 3 independent Model Universe sample cluster populations, each of size $N_{\text{samp}} = 5 \times 10^5$, are constructed to obtain 3 values of the present-day event count, N_{mrg} . These, in turn, yield 6 different differential merger rate density profiles (a reference and a pessimistic rate for each N_{mrg} ; see the above mentioned study) per model set. As in the above mentioned study, the ‘moderate-Z’ metallicity-redshift dependence of Chruslinska & Nelemans (2019) is applied and the detector visibility horizon is taken at $z_{\text{max}} = 1.0$.

Fig. 6 shows the resulting present-day, differential intrinsic merger rate density profiles, dR/dM_1 , with respect to merger primary mass, within the PSN gap. Shown are the Model Universe average rates (black-filled squares) and the upper and lower limits (blue error bars) over the different model sets, at each M_1 -bin. As seen, the present-day, PSN-gap intrinsic merger rate density profiles from the model clusters well accommodate those estimated from GWTC (Abbott et al. 2021c; orange dots). However, the lower limit of the Model Universe dR/dM_1 is zero for all the mass bins in Fig. 6. The upper limit of the Model Universe present-day merger rate density of GW190521-like events is also well within the LVK-limits of the same (Abbott et al. 2022; hashed rectangle) but the corresponding average rate is deficient by several factors.

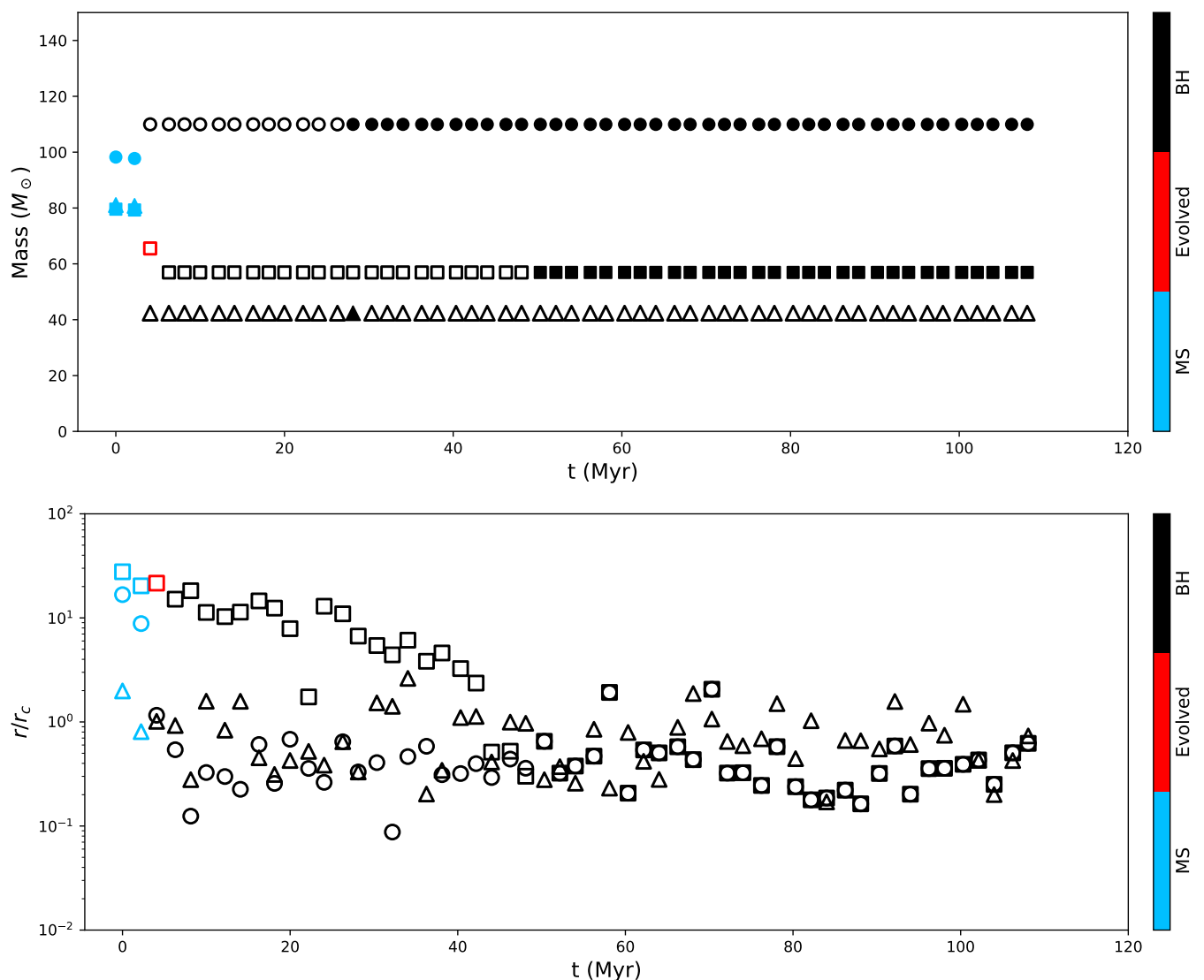


Fig. 5. The timeline of the GW190521-like merger event that occurred inside one of the computed cluster models with $W_0 = 9$, $Z = 0.0002$. In both panels the evolutions for the three cluster members, which are most relevant for the event, are shown from the start of the computation until the merger. The top panel shows the mass evolution of these objects: the trace of the merger primary and secondary mass is indicated by a circle and a square, respectively, and that of the third ‘perturber’ is represented by a triangle. The symbols are color-coded according to the stellar-evolutionary stage (main sequence, MS or beyond main sequence, Evolved or BH). If an object is a member of a binary then its symbol is filled else it is plotted empty. The bottom panel traces the radial position of these objects in units of the cluster’s instantaneous core radius r_c , r_c being determined from the cluster’s stellar distribution by applying the Casertano & Hut (1985) method. The time evolution of r_c , 10% Lagrangian radius, and half mass radius of all model clusters (Table A.1) are shown in Fig. A.1. The same symbol shapes and color coding as in the top panel are used in the bottom panel: for better visibility of overlapping symbols, the symbol filling is not applied in the bottom panel. Both the primary and the secondary BHs are born from single stars, thereby having vanishing natal spins (Sec. 2). Both the progenitor single stars are merged primordial binaries: the BH can be more massive than the plotted ZAMS progenitor depending on the mass of the latter’s companion, the age of the primordial binary’s merger, and the mass loss during the merger (Sec. 2). Although formed within the cluster well separated, the primary and secondary BHs segregate to the cluster center and pair up dynamically from ≈ 50 Myr. The third BH becomes bound to this BBH dynamically only a few Myr before the merger (lower panel). The BBH merger happens due to this triple-interaction (Samsing & Ramirez-Ruiz 2017; Banerjee 2018a, 2021a).

3.2. Rate of GW190403-like events

The present computed models also produce several BBH mergers of M_1 , M_2 , and χ_{eff} similar to GW190403, lying well within the event’s 90% confidence limits, as seen in Figs. 1, 3, and 4. In such model events, at least one of the merging BHs has $a = 1$ due to undergoing BH-TZO accretion or mass accretion in a binary (Sec. 2), prior to participating in dynamical pairing and the merger. The high χ_{eff} is due to chance alignment in dynamical pairing. Fig. 7 depicts the timeline of one of such events that occurred in one of the $W_0 = 9$, $Z = 0.005$ models.

The red-filled circles with error bars in Fig. 6 indicate the Model Universe, spin-aligned differential merger rate density of GW190403-like events, in the mass range $55M_{\odot} \lesssim M_1 \lesssim 75M_{\odot}$ over which such events occur in the computed models. These rates are obtained by multiplying the full differential rates, over the same M_1 range, with the p -value for $\chi_{\text{eff}} \geq 0.8$ of an isotropic χ_{eff} distribution corresponding to $a_1 = a_2 = 1$ and $q = 0.25$ (GW190403-like mass ratio). The Model Universe, spin aligned merger rate remains below the LVK-estimated upper limit of

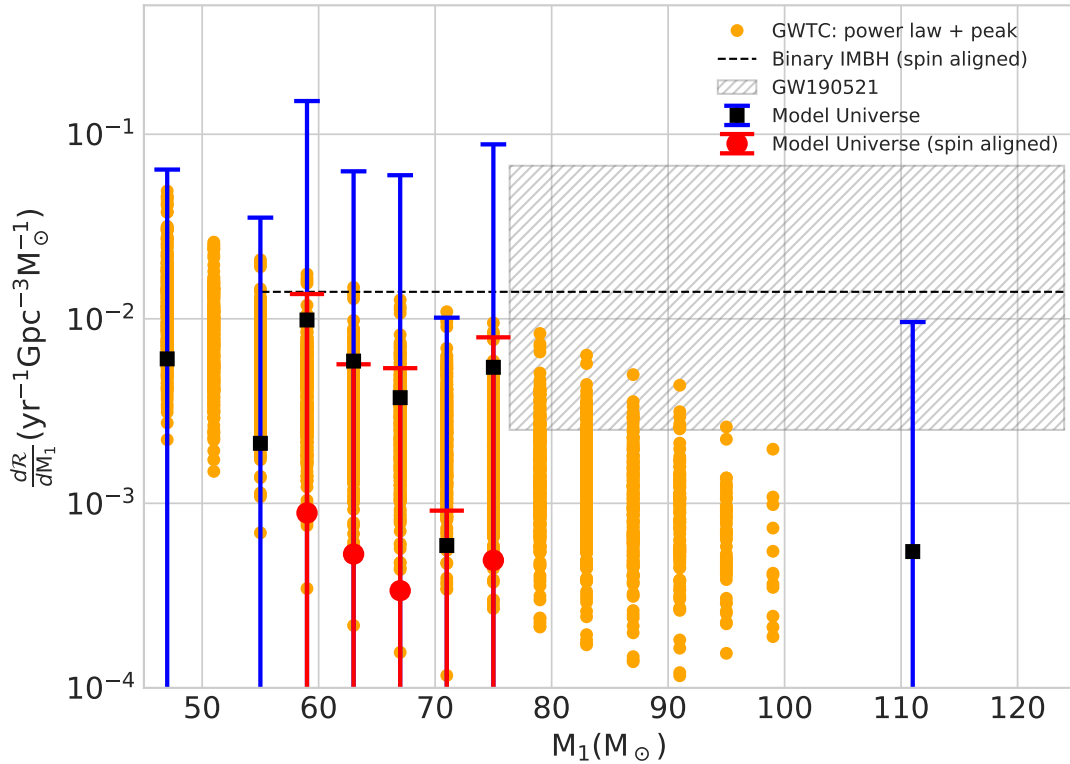


Fig. 6. The present-day, differential intrinsic BBH merger rate density (black-filled squares with blue error bars), from the Model Universe (Sec. 3.1) composed of the computed model clusters of Table A.1, as a function of merger primary mass, M_1 , within the PSN mass gap (here taken to be $45M_\odot \leq M_1 \leq 120M_\odot$). At each M_1 -bin, the average rate over the model sets (Sec. 3.1) is indicated with the black-filled square and the corresponding vertical, blue error bar indicates the maximum and minimum rates for the bin. The orange dots are random draws (300 per bin) of the posteriors of BBH differential intrinsic merger rate density, over the same range of M_1 , as obtained by the LVK (The LIGO Scientific Collaboration et al. 2021c, their power law + peak model). The hashed region spans over the 90% credible intervals of the intrinsic merger rate density of GW190521-like events and GW190521’s primary mass, as estimated by the LVK (Abbott et al. 2020; Abbott et al. 2022). The horizontal, black-dashed line indicates the LVK-estimated upper limit of the merger rate density of equal mass, aligned spin ($\chi_{\text{eff}} > 0.8$) BBHs of total mass $200M_\odot$ (Abbott et al. 2022). The line spans from the lower primary mass limit of GW190403 to the upper primary mass limit of GW190521. The red-filled circles and the corresponding vertical, red error bars represent, respectively, the average and the limits of the aligned spin fractions of the Model Universe differential BBH merger rate density over $55M_\odot \leq M_1 \leq 75.0M_\odot$. The LVK-estimated total rates are divided by the bin width ($4M_\odot$), to represent them in the $dR/dM_1 - M_1$ plane. The lower limit of the Model Universe rate is zero in each bin. Due to the logarithmic scale along the vertical axis, rate values below $10^{-4} \text{ yr}^{-1} \text{ Gpc}^{-3} M_\odot^{-1}$ are not shown in this figure.

aligned spin ($\chi_{\text{eff}} \geq 0.8$), equal mass, $200M_\odot$ IMBH-IMBH merger rate (Abbott et al. 2022; black-dashed line).

Note that the above, LVK-reported IMBH-IMBH merger rate density should be taken only as a reference upper limit in this study. Equal mass IMBH-IMBH mergers of $200M_\odot$ and high χ_{eff} neither occur in the present models nor has yet been detected by the LVK. The upper merger rate limit is inferred by the LVK based on artificially injected events (Abbott et al. 2022). As of now, LVK has not reported a merger rate that applies specifically to GW190403-like events. The vast majority of the 2G BHs (which BHs can approach $100M_\odot$ and be of high Kerr parameter) leave the clusters right after the 1G-1G BBH mergers that form them, due to the associated GW recoil kick (Sec. 2). Although $80M_\odot - 120M_\odot$ star-star-merger-product and mass-accreted BHs remain in the clusters, they get dynamically ejected within ≤ 100 Myr (Fig. 2) unless they get engaged in a massive 1G merger (Sec. 3.1).

Table 1 lists the Model Universe limits of the present day, intrinsic merger rate densities of the various event types. The lower limit of these total rates and as well of the differential rates (see above) is zero since some of the cluster model sets used in the population synthesis (Sec. 3.1) do not produce any PSN-gap BBH mergers. The set to set variation of the merger yield also re-

sults in the rather large uncertainty in the Model Universe differential rate profile within the PSN gap (Fig. 6). The rate densities of GW190403- and GW190521-type events in Table 1 incorporate only those fractions of Model Universe mergers whose M_1 , M_2 , and χ_{eff} all lie within the 90% credible intervals of the respective event parameters.

4. Summary and concluding remarks

This study investigates dynamical interactions among stars and BHs in YMCs as a potential mechanism for forming BHs within the PSN mass gap and engaging them in GR mergers. To that end, evolutionary models of YMCs (Sec. 2, Table A.1) of representative initial mass and size $7.5 \times 10^4 M_\odot$ and 2 pc, respectively, are explored. The model clusters also include an observationally-motivated population of primordial binaries. The model evolutions are computed with an updated version of the direct N-body code NBODY7 that incorporates up to date schemes of stellar mass loss, stellar remnant formation, BH natal spin, and GR-merger recoil.

These computed models produce BBH mergers that are well consistent with the merger masses (M_1, M_2) of the GWTC events (Sec. 3; Fig. 1). This is as well true for the evolutionary cluster

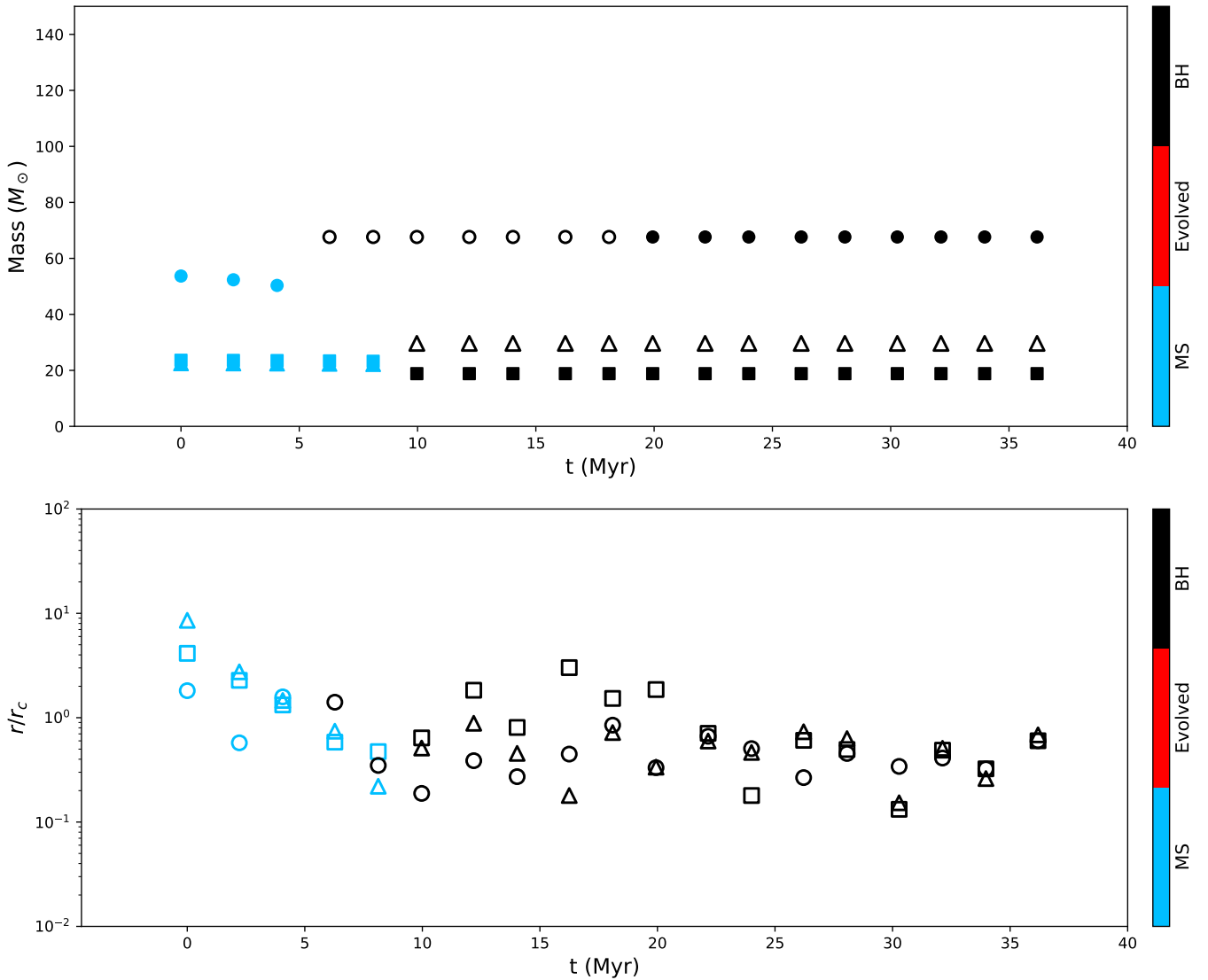


Fig. 7. The timeline of a GW190403-like merger event that occurred inside one of the computed cluster models with $W_0 = 9$, $Z = 0.005$. The meanings of the symbols are the same as in Fig. 5. Here, early in the cluster evolution, the merger primary BH is born in a primordial binary and gains mass via BH-TZO accretion from its stellar companion. The merger secondary BH is born in a symbiotic binary. This is how both of the merging BHs become maximally spinning ($a_1 = a_2 = 1$), given the present scheme of assigning BH spins (Sec. 2). As in the example of Fig. 5, the BBH merger happens due to dynamical pairing of the merging BHs and, thereafter, a triple-interaction involving a third perturber BH. In this case, both interactions happen only a few Myr before the merger (lower panel). All other GW190403-type mergers in the present models are also in-cluster dynamical mergers involving at least one such ‘spun-up’ BH, except one which is an ejected merger (see Fig. 3).

Table 1. Intrinsic merger rate densities from the computed models.

Event type	Intrinsic merger rate density/ $\text{yr}^{-1}\text{Gpc}^{-3}$
PSN-gap	$0.0 - 8.4 \times 10^{-1}$
GW190521	$0.0 - 3.8 \times 10^{-2}$
GW190403	$0.0 - 1.6 \times 10^{-1}$

Notes. Quoted are the ranges of present-day, intrinsic rate densities of Model Universe BBH mergers (right column), that resemble specific observed GW events (left column; Fig. 4).

models of Ba21 but the present models tend to produce BBH merges involving PSN-gap BHs more efficiently, owing to their initial configurations of higher central concentration (Sec. 2, Table A.1). A high central concentration accelerates the central segregation of the most massive cluster members, thereby facilitating star-star and star-BH mergers which, in turn, facilitate the formation of PSN-gap BHs (Sec. 3 and references therein). The

model mergers’ spin-orbit alignments (χ_{eff}) are also consistent with the to-date LVK events (Fig. 3). In particular, the present models do produce BBH mergers resembling GW190521 and GW190403, in all aspects (M_1 , q , χ_{eff} ; Fig. 4).

Here, the large, $\approx 100M_{\odot}$, component masses and vanishing χ_{eff} of the GW190521-like event arise due to involvement of BHs derived directly from star-star merger products whose

BHs have zero natal spins (Secs. 2, 3.1). In contrast, the high χ_{eff} of the GW190403-like events is due to involvement of BHs that are spun-up via matter accretion (via mass transfer in a binary or from a BH-TZO) or being a former member of a tidally-interacting binary (Secs. 2, 3.2). The high central concentration and efficient mass segregation in the model clusters also facilitate the high mass-asymmetry (see Ba21) in the GW190403-type mergers. The present models produce mergers of mass ratio down to ≈ 0.25 (similar to Ba21). However, beyond $M_1 \gtrsim 30M_{\odot}$, the present pure dynamical mechanism does not reproduce the bias towards $\chi_{\text{eff}} > 0$, as apparent in the LVK data (Fig. 3). This suggests contribution from additional merger channels; *e.g.*, isolated evolution of field massive binaries (*e.g.*, Belczynski et al. 2020b; Wong et al. 2021; Olejak & Belczynski 2021). Further GW events and improved spin measurement in GW observations will better suggest the channel(s) for BBH mergers of high χ_{eff} magnitudes like GW190403.

The key uncertainties in the cluster model ingredients are the adopted small star-star merger mass loss and large BH-TZO accretion fractions ($\leq 10\%$ and 95% , respectively; see Sec. 2). These settings optimize massive BH formation in the computed cluster models. Some support for a $\lesssim 10\%$ mass loss in a star-star merger come from ‘sticky-star’-type hydrodynamic calculations (*e.g.*, Lombardi et al. 2002; Gaburov et al. 2008). The nature of BH-TZO and the resulting matter accretion onto the BH is, currently, mostly elusive. However, an analogy with the direct collapse BH formation scenario may provide qualitative justification to the assumed high BH-TZO accretion (Banerjee 2019). Another important uncertainty is the spin-up of BHs: at present, all BHs undergoing potential scenarios for gaining angular momentum (mass transfer from a stellar companion, membership of a symbiotic binary, BH-TZO accretion) are assigned the maximal spin ($a = 1$) irrespective of the BH’s natal spin (Sec. 2). Angular momentum deposition onto a BH is, largely, poorly understood and the setting of $a = 1$ is likely an extremization. A qualitative basis for this model setting is that the typical spin angular momentum of a star (*e.g.*, Lang 1992; Hurley et al. 2000) or orbital angular momentum of a massive-stellar binary (*e.g.*, Tauris et al. 2017) is much higher than that of a maximally spinning stellar mass BH⁵.

The GW-merger recoil of the 2G BHs, as incorporated in the present models based on recent NR results (Sec. 2), ejects most of them from these model clusters which have moderate, $v_{\text{esc}} \approx 40 \text{ km s}^{-1}$, central escape speed. This is why 2G BBH mergers do not contribute to highly aligned, PSN-gap BBH mergers (GW190403-type events) or any other GR merger involving a highly spinning BH, in the present YMC models. (The much larger number of and much longer term evolutionary cluster models in Ba21 have produced a few 2G BBH mergers.) Note, however, that in galactic nuclear clusters, where $v_{\text{esc}} \gtrsim$

100 km s^{-1} , 2G BHs are more likely to engage in hierarchical BBH mergers despite their GW recoil (Mahapatra et al. 2021), which BHs can even be of $\approx 100M_{\odot}$ and low spin (Antonini et al. 2019; Belczynski & Banerjee 2020).

The present YMC models, nevertheless, well accommodate the LVK present-day, differential intrinsic BBH merger rate density within the PSN gap (Sec. 3.1, Fig. 6). The aligned-spin ($\chi_{\text{eff}} > 0.8$) fraction of GW190403-type mergers, as obtained from these models, make up a present-day rate density that is consistent with the LVK-estimated reference upper limit of the rate density of $200M_{\odot}$, equal-mass, aligned-spin BBH mergers (Sec. 3.2, Fig. 6). These results suggest that the tandem of massive binary evolution and dynamical interactions in $\lesssim 100 \text{ Myr}$ old YMCs can plausibly produce BBH mergers involving BHs within the PSN gap and in rates consistent with what is inferred from to-date GW observations.

However, the merger rate density of GW190521-like events from the present models ($0 - \approx 3.8 \times 10^{-2} \text{ yr}^{-1} \text{ Gpc}^{-3}$) is small compared to the models’ overall PSN-gap BBH merger rate density (Table 1, Fig. 6). Also, the model merger rate density of GW190521-like events fail to reach LVK’s upper limit of the same, as opposed to the comparison for the less massive PSN-gap mergers, and its average value is several factors smaller than the LVK’s lower limit (see Fig. 6). This means that the present YMC models are rather inefficient in producing GW190521-type mergers (see also Fragione & Banerjee 2021), although the upper limit of such events’ yield is still consistent with and within range of the corresponding LVK-estimated rate limits. Alternative formation channels (see Sec. 1 and references therein) may be more efficient in producing such massive BBH mergers.

Note that the results presented here do not comprise a ‘full story’ but represent the yield from YMCs. The modelled clusters represent the most massive young clusters that we observe, *e.g.*, R136, Westerlund 1. Also, the clusters are evolved up to 300 Myr, when they are still in their young phase, dense, and contain a substantial BH population. They would, therefore, continue to produce late-time GR mergers as they evolve into open clusters, as seen in Ba21. In the near future, such a cluster model set with a range of mass, size, and long-term evolution will be investigated.

Acknowledgements. The author (SB) thanks the reviewer for criticisms and suggestions that have improved the paper. SB acknowledges support from the Deutsche Forschungsgemeinschaft (DFG; German Research Foundation) through the individual research grant ‘‘The dynamics of stellar-mass black holes in dense stellar systems and their role in gravitational-wave generation’’ (BA 4281/6-1; PI: S. Banerjee). SB acknowledges the generous support and efficient system maintenance of the computing teams at the AIfA and HISKP. This work and the illustrations presented therein are greatly benefited by the use of the Python packages NumPy, SciPy, and Matplotlib. This work has been benefited by discussions with Aleksandra Olejak, Francesco Rizzuto, Chris Belczynski, Giacomo Fragione, Kyle Kremer, Fabio Antonini, Mark Gieles, Thorsten Naab, Jeremiah Ostriker, and Rainer Spurzem. SB has solely performed, managed, and analysed all the N-body computations presented in this work. SB has done all the coding necessary for this work, prepared the illustrations, and written the manuscript.

References

- Aarseth, S. J. 2012, MNRAS, 422, 841
- Aasi, J., Abbott, B. P., Abbott, R., et al. 2015, Classical and Quantum Gravity, 32, 074001
- Abbott, B. P., Abbott, R., Abbott, T. D., et al. 2016, Physical Review Letters, 116, 061102
- Abbott, B. P., Abbott, R., Abbott, T. D., et al. 2019, Physical Review X, 9, 031040
- Abbott, R., Abbott, T. D., Abraham, S., et al. 2021a, Phys. Rev. X, 11, 021053
- Abbott, R., Abbott, T. D., Abraham, S., et al. 2021b, ApJ, 915, L5
- Abbott, R., Abbott, T. D., Abraham, S., et al. 2021c, ApJ, 913, L7

⁵ Of course, $a = 1$ represents the extremal value of the Kerr parameter and this value is often taken to represent a highly or near maximally spinning BH. In reality, the exact value of unity won’t be achieved since an increasing specific angular momentum of the BH would also enhance angular momentum draining via, *e.g.*, outflow of the accreting matter or GW radiation. However, any value of a infinitesimally close to unity is feasible and in astrophysical scenarios a can become practically unity (see, *e.g.*, Kesden 2008; Benson & Babul 2009). Since there is no physical bound on how close to unity a can get as a BH continues to accrete angular momentum from its surrounding or companion, $a = 1$ can be taken as a representative of a BH that is subjected to a reservoir of angular momentum. In practice, taking $a = 1$ or close to 1 will cause a negligible difference to the present results (see, *e.g.*, Arca Sedda et al. 2021).

- Abbott, R., Abbott, T. D., Abraham, S., et al. 2020, *Phys. Rev. Lett.*, 125, 101102
- Abbott, R., Abbott, T. D., Acernese, F., et al. 2022, *A&A*, 659, A84
- Acernese, F., Agathos, M., Agatsuma, K., et al. 2015, *Classical and Quantum Gravity*, 32, 024001
- Ajith, P., Hannam, M., Husa, S., et al. 2011, *Phys. Rev. Lett.*, 106, 241101
- Antonini, F., Gieles, M., & Gualandris, A. 2019, *MNRAS*, 486, 5008
- Arca Sedda, M., Mapelli, M., Benacquista, M., & Spera, M. 2021, arXiv e-prints, arXiv:2109.12119
- Arca Sedda, M., Mapelli, M., Spera, M., Benacquista, M., & Giacobbo, N. 2020, *ApJ*, 894, 133
- Baibhav, V., Berti, E., Gerosa, D., Mould, M., & Wong, K. W. K. 2021, *Phys. Rev. D*, 104, 084002
- Baibhav, V., Gerosa, D., Berti, E., et al. 2020, *Phys. Rev. D*, 102, 043002
- Banerjee, S. 2017, *MNRAS*, 467, 524
- Banerjee, S. 2018a, *MNRAS*, 481, 5123
- Banerjee, S. 2018b, *MNRAS*, 473, 909
- Banerjee, S. 2019, arXiv e-prints, arXiv:1912.06022
- Banerjee, S. 2021a, *MNRAS*, 500, 3002
- Banerjee, S. 2021b, *MNRAS*, 503, 3371
- Banerjee, S. 2022, *Phys. Rev. D*, 105, 023004
- Banerjee, S., Baumgardt, H., & Kroupa, P. 2010, *MNRAS*, 402, 371
- Banerjee, S., Belczynski, K., Fryer, C. L., et al. 2020, *A&A*, 639, A41
- Banerjee, S. & Kroupa, P. 2018, *Astrophysics and Space Science Library*, Vol. 424, *Formation of Very Young Massive Clusters and Implications for Globular Clusters*, ed. S. Stahler, 143
- Belczynski, K. 2020, *ApJ*, 905, L15
- Belczynski, K. & Banerjee, S. 2020, *A&A*, 640, L20
- Belczynski, K., Heger, A., Gladysz, W., et al. 2016, *A&A*, 594, A97
- Belczynski, K., Hirschi, R., Kaiser, E. A., et al. 2020a, *ApJ*, 890, 113
- Belczynski, K., Klencki, J., Fields, C. E., et al. 2020b, *A&A*, 636, A104
- Benson, A. J. & Babul, A. 2009, *MNRAS*, 397, 1302
- Branchesi, M. 2016, in *Journal of Physics Conference Series*, Vol. 718, *Journal of Physics Conference Series*, 022004
- Carr, B. & Silk, J. 2018, *MNRAS*, 478, 3756
- Casertano, S. & Hut, P. 1985, *ApJ*, 298, 80
- Chruslinska, M. & Nelemans, G. 2019, *MNRAS*, 488, 5300
- Clesse, S. & García-Bellido, J. 2017, *Physics of the Dark Universe*, 15, 142
- Costa, G., Bressan, A., Mapelli, M., et al. 2021, *MNRAS*, 501, 4514
- De Luca, V., Desjacques, V., Franciolini, G., Malhotra, A., & Riotto, A. 2019, *J. Cosmology Astropart. Phys.*, 2019, 018
- Di Carlo, U. N., Mapelli, M., Bouffanais, Y., et al. 2020a, *MNRAS*, 497, 1043
- Di Carlo, U. N., Mapelli, M., Giacobbo, N., et al. 2020b, *MNRAS*, 498, 495
- Duquennoy, A. & Mayor, M. 1991, *A&A*, 248, 485
- Edelman, B., Doctor, Z., & Farr, B. 2021, *The Astrophysical Journal Letters*, 913, L23
- Farmer, R., Renzo, M., de Mink, S. E., Fishbach, M., & Justham, S. 2020, *ApJ*, 902, L36
- Fragione, G. & Banerjee, S. 2021, *ApJ*, 913, L29
- Fragione, G., Loeb, A., & Rasio, F. A. 2020, *ApJ*, 895, L15
- Fryer, C. L., Belczynski, K., Wiktorowicz, G., et al. 2012, *ApJ*, 749, 91
- Fuller, J. & Ma, L. 2019, *ApJ*, 881, L1
- Gaburov, E., Lombardi, J. C., & Portegies Zwart, S. 2008, *MNRAS*, 383, L5
- Gerosa, D. & Fishbach, M. 2021, *Nature Astronomy*, 5, 749
- Glebbeek, E., Gaburov, E., de Mink, S. E., Pols, O. R., & Portegies Zwart, S. F. 2009, *A&A*, 497, 255
- González, E., Kremer, K., Chatterjee, S., et al. 2021, *ApJ*, 908, L29
- Hammers, A. S., Fragione, G., Neunteufel, P., & Kocsis, B. 2021, *MNRAS*, 506, 5345
- Heggie, D. & Hut, P. 2003, *The Gravitational Million-Body Problem: A Multi-disciplinary Approach to Star Cluster Dynamics*
- Hofmann, F., Barausse, E., & Rezzolla, L. 2016, *ApJ*, 825, L19
- Hurley, J. R., Pols, O. R., & Tout, C. A. 2000, *Monthly Notices of the Royal Astronomical Society*, 315, 543
- Hurley, J. R., Tout, C. A., & Pols, O. R. 2002, *Monthly Notices of the Royal Astronomical Society*, 329, 897
- KAGRA Collaboration, Akutsu, T., Ando, M., et al. 2020, *Progress of Theoretical and Experimental Physics*, 2021 [arXiv:2008.02921], 05A103
- Katz, B., Dong, S., & Malhotra, R. 2011, *Physical Review Letters*, 107, 181101
- Kerr, R. P. 1963, *Phys. Rev. Lett.*, 11, 237
- Kesden, M. 2008, *Phys. Rev. D*, 78, 084030
- King, I. R. 1966, *AJ*, 71, 64
- Kozai, Y. 1962, *The Astronomical Journal*, 67, 591
- Kroupa, P. 2001, *MNRAS*, 322, 231
- Krumholz, M. R., McKee, C. F., & Bland-Hawthorn, J. 2019, *ARA&A*, 57, 227
- Kuhn, M. A., Povich, M. S., Luhman, K. L., et al. 2013, *ApJS*, 209, 29
- Lang, K. R. 1992, *Astrophysical Data I. Planets and Stars*
- Langer, N., Norman, C. A., de Koter, A., et al. 2007, *A&A*, 475, L19
- Lithwick, Y. & Naoz, S. 2011, *ApJ*, 742, 94
- Lombardi, James C., J., Warren, J. S., Rasio, F. A., Sills, A., & Warren, A. R. 2002, *ApJ*, 568, 939
- Lousto, C. O., Zlochower, Y., Dotti, M., & Volonteri, M. 2012, *Phys. Rev. D*, 85, 084015
- Mahapatra, P., Gupta, A., Favata, M., Arun, K. G., & Sathyaprakash, B. S. 2021, *ApJ*, 918, L31
- Mandel, I. & Broekgaarden, F. S. 2022, *Living Reviews in Relativity*, 25, 1
- Mapelli, M. 2018, in *Journal of Physics Conference Series*, Vol. 957, *Journal of Physics Conference Series*, 012001
- Mapelli, M., Santoliquido, F., Bouffanais, Y., et al. 2021, *Symmetry*, 13, 1678
- Mapelli, M., Spera, M., Montanari, E., et al. 2020, *ApJ*, 888, 76
- Mathieu, R. D. 2000, in *Astronomical Society of the Pacific Conference Series*, Vol. 198, *Stellar Clusters and Associations: Convection, Rotation, and Dynamics*, ed. R. Pallavicini, G. Micela, & S. Sciortino, 517
- Mészáros, P., Fox, D. B., Hanna, C., & Murase, K. 2019, *Nature Reviews Physics*, 1, 585
- Mikkola, S. & Merritt, D. 2008, *The Astronomical Journal*, 135, 2398
- Mikkola, S. & Tanikawa, K. 1999, *Monthly Notices of the Royal Astronomical Society*, 310, 745
- Moe, M. & Di Stefano, R. 2017, *ApJS*, 230, 15
- Morscher, M., Pattabiraman, B., Rodriguez, C., Rasio, F. A., & Umbreit, S. 2015, *The Astrophysical Journal*, 800, 9
- O'Brien, B., Szczeptańczyk, M., Gayathri, V., et al. 2021, *Phys. Rev. D*, 104, 082003
- Olejak, A. & Belczynski, K. 2021, *ApJ*, 921, L2
- Perna, R., Wang, Y.-H., Farr, W. M., Leigh, N., & Cantiello, M. 2019, *ApJ*, 878, L1
- Plummer, H. C. 1911, *MNRAS*, 71, 460
- Portegies Zwart, S. F. & McMillan, S. L. W. 2000, *ApJ*, 528, L17
- Portegies Zwart, S. F., McMillan, S. L. W., & Gieles, M. 2010, *ARA&A*, 48, 431
- Rastello, S., Mapelli, M., Di Carlo, U. N., et al. 2021, *MNRAS*, 507, 3612
- Rizzuto, F. P., Naab, T., Spurzem, R., et al. 2022, *MNRAS*, 512, 884
- Rizzuto, F. P., Naab, T., Spurzem, R., et al. 2021, *MNRAS*, 501, 5257
- Rodriguez, C. L., Amaro-Seoane, P., Chatterjee, S., & Rasio, F. A. 2018, *Phys. Rev. Lett.*, 120, 151101
- Roupas, Z. & Kazanas, D. 2019, *A&A*, 632, L8
- Samsing, J. & Ramirez-Ruiz, E. 2017, *ApJ*, 840, L14
- Sana, H., de Koter, A., de Mink, S. E., et al. 2013, *A&A*, 550, A107
- Sana, H. & Evans, C. J. 2011, in *IAU Symposium*, Vol. 272, *Active OB Stars: Structure, Evolution, Mass Loss, and Critical Limits*, ed. C. Neiner, G. Wade, G. Meynet, & G. Peters, 474–485
- Sigurdsson, S. & Hernquist, L. 1993, *Nature*, 364, 423
- Spera, M., Mapelli, M., Giacobbo, N., et al. 2019, *MNRAS*, 485, 889
- Spitzer, L. 1987, *Dynamical evolution of globular clusters*, Princeton University Press, Princeton, NJ, 191 p.
- Tanikawa, A., Kinugawa, T., Yoshida, T., Hijikawa, K., & Umeda, H. 2021a, *MNRAS*, 505, 2170
- Tanikawa, A., Susa, H., Yoshida, T., Trani, A. A., & Kinugawa, T. 2021b, *ApJ*, 910, 30
- Tauris, T. M., Kramer, M., Freire, P. C. C., et al. 2017, *ApJ*, 846, 170
- The LIGO Scientific Collaboration, the Virgo Collaboration, Abbott, R., et al. 2021a, arXiv e-prints, arXiv:2108.01045
- The LIGO Scientific Collaboration, the Virgo Collaboration, the KAGRA Collaboration, et al. 2021b, arXiv e-prints, arXiv:2111.03606
- The LIGO Scientific Collaboration, the Virgo Collaboration, the KAGRA Collaboration, et al. 2021c, arXiv e-prints, arXiv:2111.03634
- Thorne, K. S. & Zytkov, A. N. 1975, *ApJ*, 199, L19
- Vigna-Gómez, A., Toonen, S., Ramirez-Ruiz, E., et al. 2021, *ApJ*, 907, L19
- Vink, J. S., Higgins, E. R., Sander, A. A. C., & Sabhahit, G. N. 2021, *MNRAS*, 504, 146
- Webb, J. J. & Sills, A. 2021, *MNRAS*, 501, 1933
- Wong, K. W. K., Breivik, K., Kremer, K., & Callister, T. 2021, *Phys. Rev. D*, 103, 083021
- Woosley, S. E. 2017, *ApJ*, 836, 244
- Woosley, S. E. & Heger, A. 2021, *ApJ*, 912, L31
- Woosley, S. E., Sukhbold, T., & Janka, H. T. 2020, *ApJ*, 896, 56
- Ziegler, J. & Freese, K. 2021, *Phys. Rev. D*, 104, 043015

Appendix A: Direct N-body runs of model star clusters
Table A.1. Summary of the new direct N-body evolutionary models of star clusters and their GR-merger yields in this work.

No.	M_{cl}/M_{\odot}	r_h/pc	W_0	Z	f_{bin}	$T_{\text{evol}}/\text{Myr}$	remnant model	SN kick	BH spin	$N_{\text{mrg.in}}$	$N_{\text{mrg.out}}$
1	⁶ 7.5×10^4	2.0	7.0	0.0002	0.05 ⁷	300.0	rapid+B16	mom. cons. ⁸	FM19 ⁹	0	3
2										0	1
3										0	1
4										2	2
5	7.5×10^4	2.0	7.0	0.001	0.05	300.0	rapid+B16	mom. cons.	FM19	1	3
6										2	1
7										0	1
8										1	0
9	7.5×10^4	2.0	7.0	0.005	0.05	300.0	rapid+B16	mom. cons.	FM19	0	1
10										0	0
11										0	1
12										0	0
13	7.5×10^4	2.0	7.0	0.01	0.05	300.0	rapid+B16	mom. cons.	FM19	0	0
14										1	0
15										0	0
16										0	0
17	7.5×10^4	2.0	7.0	0.02	0.05	300.0	rapid+B16	mom. cons.	FM19	0	1
18										0	0
19										1	0
20										0	0
21	7.5×10^4	2.0	9.0	0.0002	0.05	300.0	rapid+B16	mom. cons.	FM19	1	2
22										2	3
23										0	0
24										0	1
25	7.5×10^4	2.0	9.0	0.001	0.05	300.0	rapid+B16	mom. cons.	FM19	1	0
26										1	1
27										0	1
28										0	1
29	7.5×10^4	2.0	9.0	0.005	0.05	300.0	rapid+B16	mom. cons.	FM19	2	1
30										1	1
31										0	0
32										1	1
33	7.5×10^4	2.0	9.0	0.01	0.05	300.0	rapid+B16	mom. cons.	FM19	0	0

Continued on next page

⁶ Initial number of stars $N \approx 1.28 \times 10^5$
⁷ The binary fraction is defined as $f_{\text{bin}} = 2N_{\text{bin}}/N$, N_{bin} being the total number of binaries and N being the total number of members. Note that the initial binary fraction among the O stars, considered separately, is $f_{\text{Obin}} = 1.0$ as opposed to the smaller *overall* binary fraction, f_{bin} .

⁸ Momentum conserving natal kick as in Ba20.

⁹ Vanishing BH natal spins (Fuller & Ma 2019).

Table A.1 – continued from previous page

No.	M_{cl}/M_{\odot}	r_{h}/pc	W_0	Z	f_{bin}	$T_{\text{evol}}/\text{Myr}$	remnant model	SN kick	BH spin	$N_{\text{mrg.in}}$	$N_{\text{mrg.out}}$
34										1	0
35										0	0
36										1	0
37	7.5×10^4	2.0	9.0	0.02	0.05	300.0	rapid+B16	mom. cons.	FM19	0	0
38										0	0
39										0	0
40										0	0

Note: The columns from left to right give the model cluster’s ID number, initial mass, M_{cl} , initial half-mass radius, r_{h} , initial King concentration parameter, W_0 , metallicity, Z , initial overall fraction of primordial binaries, f_{bin} , model evolutionary time, T_{evol} , remnant-mass and PPSN/PSN model, remnant natal kick model, BH natal spin model, number of GR mergers within the cluster, $N_{\text{mrg.in}}$, number of GR mergers after getting ejected from the cluster, $N_{\text{mrg.out}}$.

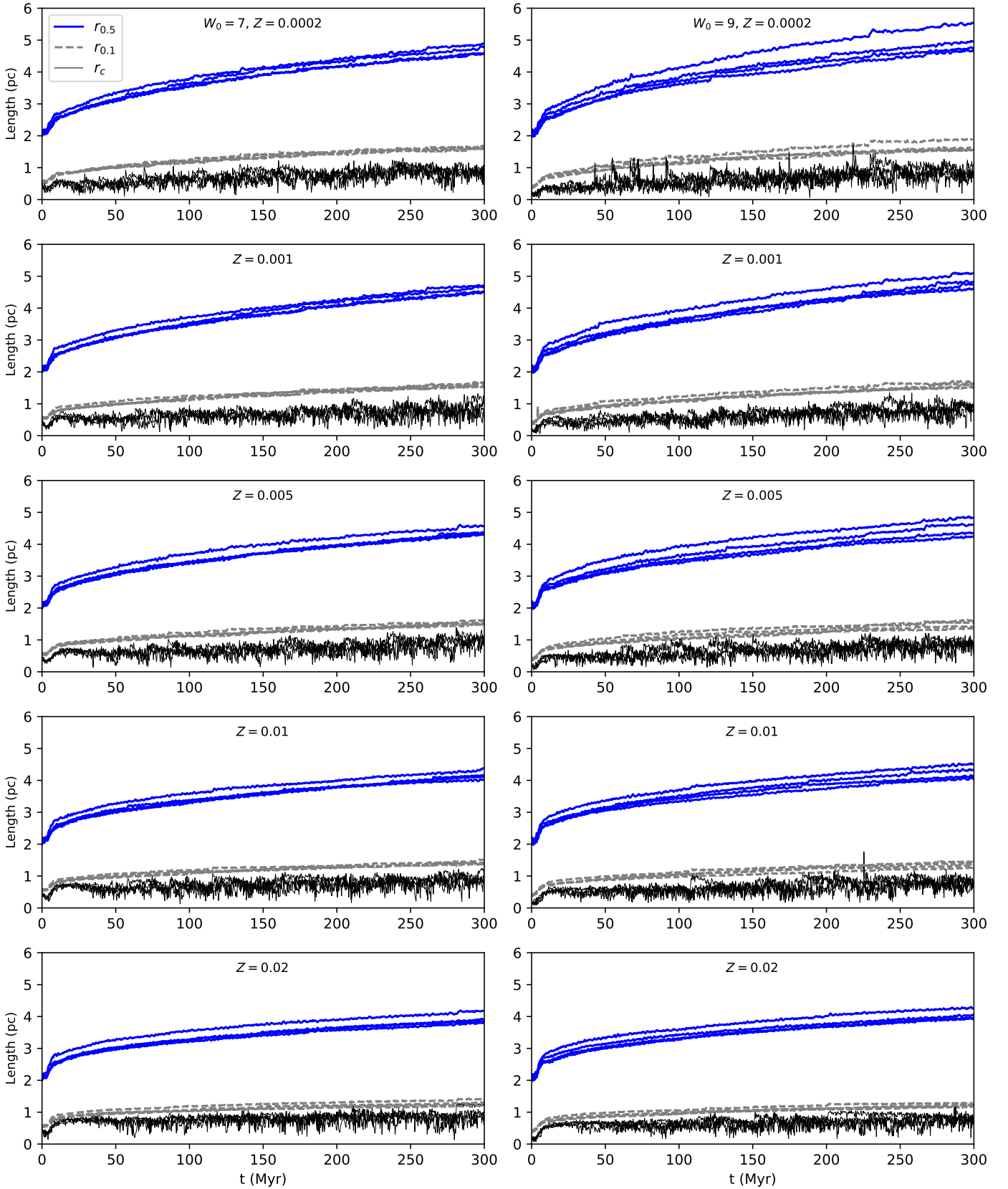


Fig. A.1. The time evolution of the core radius, r_c , 10% Lagrangian radius, $r_{0.1}$, and 50% Lagrangian radius (half mass radius), $r_{0.5}$, of all the computed cluster models in Table A.1. The panels in the left (right) column correspond to the models with $W_0 = 7$ ($W_0 = 9$) with Z as indicated in each panel's title. $r_c(t)$, $r_{0.1}(t)$, and $r_{0.5}(t)$ (legend) are plotted for each model separately.